



## Synchronized Oscillation in Coupled Nanomechanical Oscillators

Seung-Bo Shim, *et al.*  
*Science* **316**, 95 (2007);  
DOI: 10.1126/science.1137307

**The following resources related to this article are available online at [www.sciencemag.org](http://www.sciencemag.org) (this information is current as of April 5, 2007):**

**Updated information and services**, including high-resolution figures, can be found in the online version of this article at:

<http://www.sciencemag.org/cgi/content/full/316/5821/95>

**Supporting Online Material** can be found at:

<http://www.sciencemag.org/cgi/content/full/316/5821/95/DC1>

This article **cites 17 articles**, 1 of which can be accessed for free:

<http://www.sciencemag.org/cgi/content/full/316/5821/95#otherarticles>

This article appears in the following **subject collections**:

Physics, Applied

[http://www.sciencemag.org/cgi/collection/app\\_physics](http://www.sciencemag.org/cgi/collection/app_physics)

Information about obtaining **reprints** of this article or about obtaining **permission to reproduce this article** in whole or in part can be found at:

<http://www.sciencemag.org/about/permissions.dtl>

15. K. Tanaka, E. Kolb, *U.S. Geol. Surv. Open-File Rep.* 2005-1271 (2005).  
 16. R. Sibson, in *Interpolating Multivariate Data* (Wiley, New York, 1981), pp. 21–36.  
 17. We used the natural-neighbor interpolation as implemented in the ArcMap GIS software from ESRI (Redlands, CA). The interpolation applies a weighted moving average and is a preferred method for irregularly distributed data sets (16).  
 18. C. Davies, B. A. Murray, J. Byrne, *Eos* 85, Fall Meeting Supplement, abstr. P13A-0971 (2004).  
 19. The error on this estimate includes a 10% uncertainty in refractive index and an additional factor due to gaps in coverage and detectability of the basal interface.  
 20. P. M. Schenk, J. M. Moore, *J. Geophys. Res.* 105, 24529 (2000).  
 21. S. Byrne, A. P. Ingersoll, *Science* 299, 1051 (2003).  
 22. J.-P. Bibring *et al.*, *Nature* 428, 627 (2004).  
 23. The authors acknowledge the support of the space agencies of Italy (Agenzia Spaziale Italiana), the United States (NASA), and Europe (European Space

Agency) for the operations of MARSIS and Mars Express. We thank Y. Gim for clutter simulation. Some of the research described in this publication was carried out at the Jet Propulsion Laboratory, California Institute of Technology.

8 January 2007; accepted 27 February 2007  
 Published online 15 March 2007;  
 10.1126/science.1139672  
 Include this information when citing this paper.

# Synchronized Oscillation in Coupled Nanomechanical Oscillators

Seung-Bo Shim,\* Matthias Imboden, Pritiraj Mohanty†

We report measurements of synchronization in two nanomechanical beam oscillators coupled by a mechanical element. We charted multiple regions of frequency entrainment or synchronization by their corresponding Arnold’s tongue diagrams as the oscillator was driven at subharmonic and rational commensurate frequencies. Demonstration of multiple synchronized regions could be fundamentally important to neurocomputing with mechanical oscillator networks and nanomechanical signal processing for microwave communication.

The concept of synchronized oscillation in coupled systems is pervasive in both nature (1) and human physiology (2). Examples of synchronization include rhythmic blinking of fireflies (3), the activity of pacemaker cells in the sinoatrial node of a human heart (4), and the spin-orbit resonance of the planet Mercury (5). In physical systems, synchronization has been studied for over three centuries, starting

with Huygens’ discovery of the phenomenon in two coupled pendulum clocks (6) and leading to modern-day experiments on coherent radiation in coupled spin-torque nano-oscillators (7, 8) and parametric resonance in mechanical oscillators (9, 10).

Frequency entrainment, a class of synchronization, of coupled micro- and nanomechanical oscillators is of fundamental and technical

interest. A two-oscillator system demonstrates inherently rich linear and nonlinear dynamics, which contrast with its deceptive simplicity (1, 11). After the historical observation of synchronization of two pendulum clocks by Huygens, Appleton (12) and van der Pol (13) showed that the frequency of a triode generator can be entrained, or synchronized, to an external drive; their work was motivated by the potential application in radio communication. The first systematic studies of synchronization in biological systems (and, in particular, human physiology) started with Peskin’s attempt to model self-synchronization of cardiac pacemaker cells to understand the generation of a heartbeat (4). In biological neurocomputing, neural networks show rhythmic behavior, exemplified in many

Department of Physics, Boston University, 590 Commonwealth Avenue, Boston, MA 02215, USA.

\*Present address: Center for Strongly Correlated Materials Research and School of Physics and Astronomy, Seoul National University, Seoul, South Korea.

†To whom correspondence should be addressed. E-mail: mohanty@physics.bu.edu

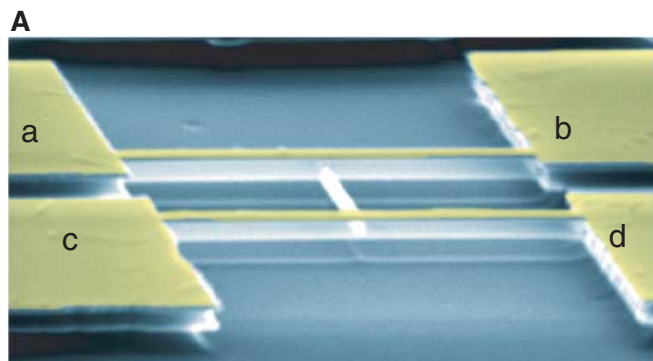
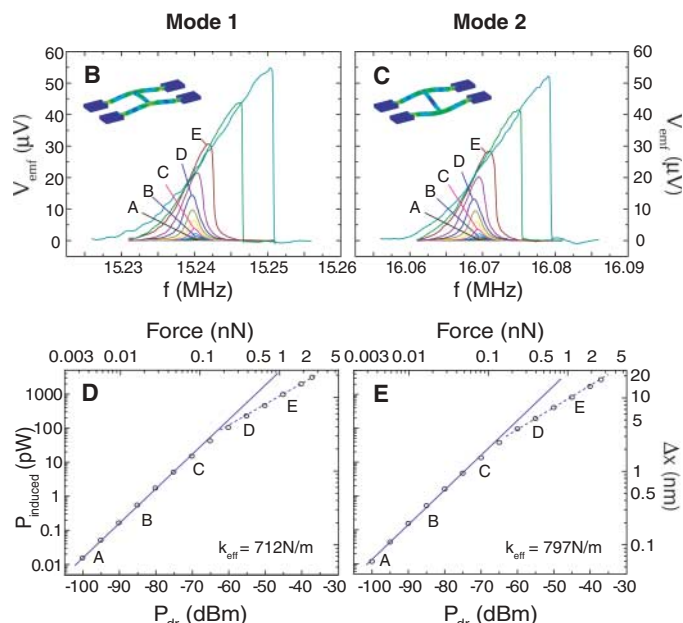


**Fig. 1.** Device micrograph, magnetomotive characterization, and mode shape. (A) Scanning electron micrograph of the coupled nanomechanical oscillator. Two main beams, each 10  $\mu\text{m}$  in length, are doubly clamped to contact pads a and b and to c and d, respectively. The main beams are mechanically coupled near the center by a 5- $\mu\text{m}$ -long beam. The beams are 500 nm wide and thick. The electrical leads (colored yellow) are selectively deposited such that contacts a and b are electrically isolated from contacts c and d. We observe two separate modes in the coupled nanomechanical resonator, labeled below as mode 1 and mode 2 with resonance frequencies of 15.241 and 16.071 MHz, respectively. (B) Linear and nonlinear response of the device structure in mode 1. The response has Lorentzian shape in the linear regime. Asymmetric responses and hysteresis occur when  $P_{\text{drive}}$  is greater than  $-60$  dBm (trace D). The inset shows the mode shape from finite element simulation.  $V_{\text{emf}}$  is the voltage measured by the network analyzer. (C) Linear and nonlinear response of the device structure in mode 2. Nonlinearity commences at similar powers as in the mode 1. (D and E)



Plots of induced power ( $P_{\text{induced}}$ ) as a response of  $P_{\text{drive}}$  at 5 T.  $P_{\text{induced}}$  is a measure of the resonant displacement, and  $P_{\text{drive}}$  corresponds to the driving force. From the log-log plot of driving force versus displacement, we calculate the effective linear-response spring constants  $k_{\text{eff}} = 712$  and  $797$  N/m for modes 1 and 2, respectively.  $\Delta x$ , the central displacement of the beam. See SOM for technical details.

brain subsystems, in which the pattern recognition properties are similar to those of oscillator networks. Therefore, with the use of networks of nanomechanical oscillators, it might be possible to build a neurocomputer with associative memory in which the network can store and retrieve complex oscillatory patterns as synchronized states (14).

Synchronized states are often represented by Arnold's tongues, which are regions of frequency locking in the parameter space. In mathematical models, these regions appear (11, 15) whenever the drive frequency  $f_d$  is a rational fraction of the resonance frequency  $f_0$ , such that  $f_d = (m/n)f_0$ , where  $m$  and  $n$  are respective integer winding numbers of two oscillators. As the coupling increases, the frequency-locking regimes widen, which give the appearance of a tongue shape. In another graphical representation, the Devil's staircase depicts the winding number of the synchronized regions as a function of  $f_d$ . This monotonic increase contains plateaus where the response frequency is locked to a given winding number. In general, the simplest fractions have the largest frequency-locked synchronized regions (16).

Another representation of synchronization is frequency entrainment, where two or many different frequencies of the oscillators, upon coupling, entrain or lock to a single frequency, determined by either the dynamics of the oscillator network or an external drive. In our experiment, we study entrainment of a given oscillator mode  $f_0$  by observing its response as another part of the structure is driven at a fractional frequency,  $f_d = (m/n)f_0$ .

Our coupled oscillator consists of two electrically independent doubly clamped beams (10  $\mu\text{m}$  long by 500 nm wide by 500 nm thick), which are coupled by a 5- $\mu\text{m}$ -long beam of the same width and thickness that is attached to the centers of the main beams (Fig. 1A). Selectively evaporated gold electrodes on each beam serve as electrical connections for measurements. Because the beams are electrically isolated, the coupling between the beams is purely mechanical. The device is fabricated from single-crystal silicon by electron-beam lithography and a combination of dry and wet etch processes. For all experimental data, the sample is cooled to 280 mK with a  $^3\text{He}$  cryostat and placed at the center of a 5 T in-plane magnetic

field. The structure is driven magnetotomatively (17) with alternating current along the beam length and perpendicular to magnetic field  $B$ . Using a network analyzer, we identify two resonances at 15.241 MHz (mode 1) and 16.071 MHz (mode 2). Corresponding mode shapes are analyzed by means of finite element simulation. Each mode has a well-defined linear and non-linear response (Fig. 1, B and C), as well as the expected  $B^2$  dependence (18). Low driving power  $P_{\text{drive}}$  measurements in the linear regime result in effective spring constants  $k_{\text{eff}}$  of 712 and 797 N/m for modes 1 and 2, respectively. From a simple point particle and spring-coupled oscillator model, the  $k_{\text{eff}}$  value of the coupling beam is estimated to be 39 N/m [see the supporting online material (SOM) for more technical details].

To observe the frequency entrainment, we drove one of the beams with a frequency generator, and the response of the second beam was measured with a spectrum analyzer at the first resonant mode [characterized by the resonant frequency of 15.241 MHz and full width at half maximum (FWHM) of 1.5 kHz]. Figure 2 shows the response at  $f_0$  when driving the beam at sub-

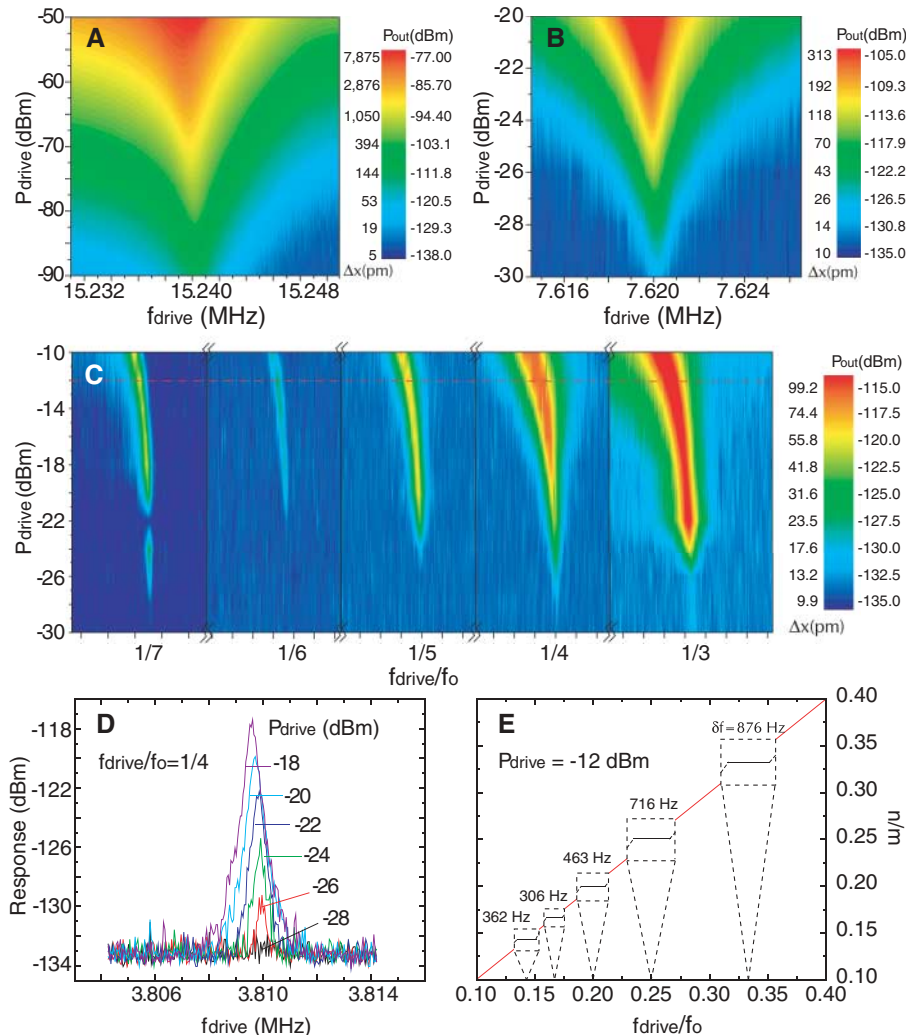


**Fig. 2.** Synchronization at subharmonic driving. Frequency-power sweep with subharmonic  $f_d$  ( $f_0/n$ ,  $n = 1, 2, \dots, 7$ ). A signal generator drives one beam, and the response of the second beam is measured with a spectrum analyzer. The contours represent the response in dBm. The synchronized regions become visible in the contour plots when the response exceeds the noise level of  $-136$  dBm. We drive one of the beams at a frequency  $f_0/n$  and record the response of the second beam at the fundamental frequency  $f_0$ . The coupling is purely mechanical as a result of the center beam (Fig. 1A). (A) Frequency-power sweep at resonant frequency  $n/m = 1$ .  $P_{\text{out}}$ , power output. (B) Synchronization with  $f_d = f_0/2$ . (C) Frequency-power sweep for subharmonic excitations ( $f_0/n$ ,  $n = 3, 4, 5, 6, 7$ ). For these measurements, a minimum of 200-dB isolation is ensured so that the higher harmonic outputs from the RF source no longer contribute. (D) Response extracted from contour plot for  $f_d = f_0/4$ . Each plot has Lorentzian shape and shows a linear increase with  $P_{\text{drive}}$ . (E) Devil's staircase plot depicting the width of the Lorentzian of each synchronized region. For clarity, the plateaus are greatly magnified. We measure FWHM ( $\delta f$ ) of the Lorentzian peaks at  $P_{\text{drive}} = -12$  dBm [dashed line in (C)]. The y axis ( $n/m$ ) represents the winding number between driving frequency and fundamental frequency.

harmonic frequencies. The observed Arnold's tongues appear at all subharmonic drive frequencies  $f_d = (1/n)f_0$  with  $n$  ranging from 1 (resonance) to 7, which means that, when the actuation frequency is an integer fraction of  $f_0$  of the first mode, this mode of the structure starts to oscillate.

Figure 2A shows the Arnold's tongue  $m/n = 1/1$  for which  $f_d$  sweeps over  $f_0$ . This is essentially the same plot as the linear part of Fig. 1B. In a typical measurement, the drive-frequency resolution is 40 Hz, and  $P_{\text{drive}}$  is increased in 2-dBm steps, which provides 10,521 averaged measurements taken over 12 hours. For the remaining Arnold's tongues (Fig. 2, B and C), low-pass filters with high isolation are used to ensure that there is no higher harmonic output from the frequency generator, because it would drive the structure on resonance. Because we do not measure the phase of the response, synchronization is detected purely through frequency locking. The term "frequency locking" is used

here rather loosely, as a synonym for resonant actuation, in which the response is measured at mode 1 and not at a single frequency; the use of the term "locked" is justified because the response frequency is correlated to a respective  $f_d$ . Resonant actuation is not observed when the drive frequency is not in the proximity of  $f_d = f_0/n$  or other well-defined drive frequencies as is seen below. The Arnold's tongues only appear with high  $P_{\text{drive}}$  where the structure is known to have nonlinear response when driven at the resonant frequency (Fig. 1).

Figure 2E displays the Devil's staircase plot, which maps the widths of the Arnold's tongues, defined as the FWHM for a given  $P_{\text{drive}}$ . Essentially, this is a slice for a given power level out of the Arnold's tongue contour plots. The actual width of frequency locking is much greater than the FWHM of the fundamental resonant mode; however, the electronic noise floor prevents detection far from the center of the Lorentzian. The  $x$  axis indicates  $f_d$ , and the  $y$  axis

represents the approximate winding number. The plateaus, representing the region of synchronization, vary in size. They tend to be larger for drive frequencies closer to  $f_0$ . However, for  $f_d = f_0/7$ , the synchronized regime is larger than the regime for  $f_d = f_0/6$ . This is not unexpected because, in a Devil's staircase, the plateau sizes do not grow monotonously.

The maximum responses in Arnold's tongues shift to lower drive frequencies for higher driving powers. Within a frequency-locked regime, the locked frequency, observed close to resonance, shifts upward with increasing  $f_d$  over a 10- to 20-kHz range. In idealized systems, Arnold's tongues are expected for every rational number  $m/n$ , where small  $m$  and  $n$  values are preferred. For this structure, drive frequencies such as  $f_d = (2/3)f_0$ ,  $(3/4)f_0$ ,  $(3/2)f_0$ , and similar fractions could not be detected within the experimental limitations. It is possible that the missing Arnold's tongues are present but are either too weak in amplitude (below the noise floor of  $-136$  dBm)

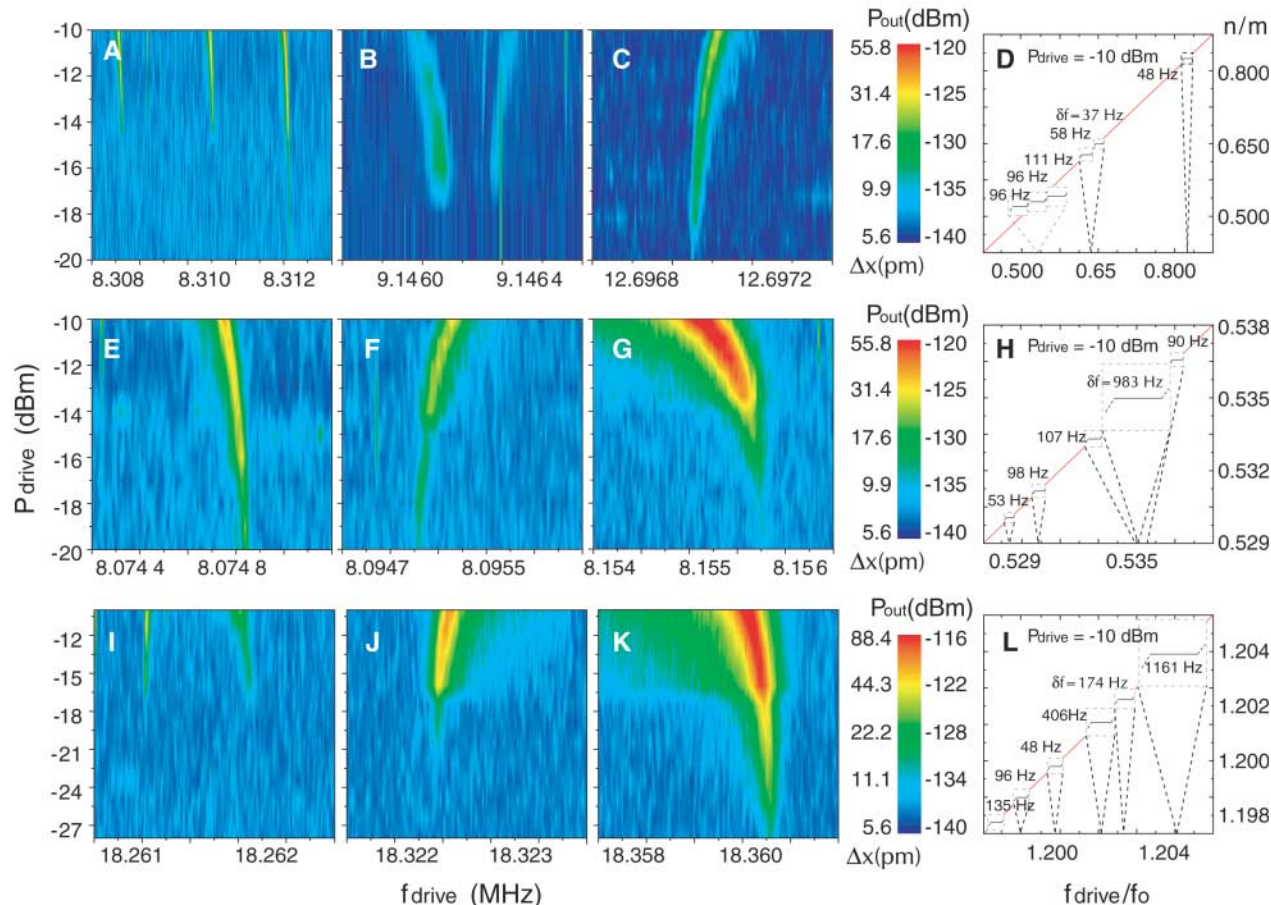


**Fig. 3.** Synchronization at non-subharmonic driving frequency. Synchronization regions other than  $f_0/n$  were discovered for a large range of frequencies by means of the same experimental procedure as in Fig. 2. In most cases [(A to C), (E) and (F), and (I) and (J)], these regions are narrow with a small response. However, two synchronization regions [(G) and (K)] were discovered to have a very prominent response, which is comparable to the  $f_0/3$  result. (G) shows subharmonic synchronization at  $f_d = 8.155$  MHz, and (K) indicates superharmonic synchronization at  $f_d = 18.360$  MHz. No obvious integer fractions can be associated with these frequencies. (D), (H),

and (L) are staircase plots indicating the widths of 16 synchronization regions. As in Fig. 2E, the plateaus have been magnified for clarity. There are two classes of synchronization regions that are characterized by their behavior when sweeping  $P_{\text{drive}}$ . In some cases, the synchronization regions appear at lower frequencies as  $P_{\text{drive}}$  increases [(A) and (B)], (E), (G), (I), and (K)] (i.e., the tongues bend to the left). However, there is also a substantial number of regions with the opposite behavior: the  $f_d$  at which frequency locking occurs increases with increasing  $P_{\text{drive}}$  [(B) and (C)], (F), and (J)] (i.e., the tongues bend to the right).

or too narrow in frequency span to be detected with our setup. Alternatively, they simply may not exist in this non-idealized setup.

In addition to the Arnold's tongues shown in Fig. 2, synchronized regions are also found at frequencies with no obvious commensurate relation to  $f_0$ . These are depicted in Fig. 3. A drive-frequency range of 370 kHz starting at 8.01 MHz, well above the  $f_d = f_0/2$  frequency, reveals 34 Arnold's tongues, with the possibility of more, where the limitations are given by the frequency resolution and preamplifier noise. A smaller drive span of 180 kHz starting at 18.24 MHz (well above  $f_0$ ) reveals a similar Arnold's tongue count of 24. Not only is resonant actuation observed, but some of these frequency-locking regimes (Fig. 3, G and K) are also larger than the synchronized regimes illustrated in Fig. 2. For both sub- and superharmonic drive frequencies, some Arnold's tongues bend down (maximum response is observed at decreasing  $f_d$ ) (Fig. 3, A, E, G, I, and K) and some Arnold's tongues bend up (maximum response is observed at increasing  $f_d$ ) (Fig. 3, C, F, and J) for growing  $P_{\text{drive}}$ . It is not clear whether there is a pattern that can be established in the data. The response frequency (i.e., the frequency at which mode 1 is observed) actually decreases as  $f_d$  increases for the Arnold's tongues that bend up. This effect is the opposite of that for the Arnold's tongues that bend down as  $P_{\text{drive}}$  increases. It is noteworthy that the bending of Arnold's tongues is also observed in mathematical simulations of phase-locked oscil-

lators as discussed in the SOM. The Devil's staircase is also plotted for these off-harmonic Arnold's tongues. The sizes of the frequency-locked regimes appear to fluctuate randomly, and no pattern could be established. A large number of frequency-locked regimes would be essential to the realization of neural computers based on oscillator networks.

Another notable aspect of nonresonant excitation is parametric amplification, which enables the enhancement of small signals in individual oscillator modes in a network. In our structure, on-chip amplification of small mechanical signals can be performed by parametric down-conversion in which the small signal generated in one beam can be amplified by coupling it to a second beam that provides the necessary pumping for signal amplification. In mechanical structures, parametric down-conversion or amplification has been studied in optical setups with cantilever (19), torsional (20), and disk resonators (21). Here, we report parametric amplification of mechanical signals in a nanometer-scale mechanical resonator with a distinct two-oscillator or two-beam structure. Parametric amplification is defined by a gain in the mechanical response on resonance (frequency  $f_0$ ) when modulating a parameter of the oscillator such as the spring constant, for instance, by adding parametric modulation (pumping) at twice the resonance frequency (pump frequency  $2f_0$ ). Because the two beams on each side of the structure are electrically isolated, we can drive the structure

through one beam and pump on the other beam. This enables us to explore purely mechanical amplification effects. In our experiment, we modulate the spring constant of the structure by applying a high-amplitude pump signal at twice the resonance frequency. We apply a pump signal ( $f_{\text{pump}} = 2f_0$ ) on one beam (c to d, Fig. 1A) while driving at  $f_0$  through the other beam (a to b, Fig. 1A). Two referenced signal generators are used for the drive and pump signals. The pre-amplified induced voltage is detected with an RF lock-in amplifier. A Lorentzian fit to the data is used to extract  $f_0$  and the amplitude  $A$ .

We observe that  $f_0$  shifts down by 1.7 kHz with an -8-dBm pump signal (Fig. 4A), possibly as a result of the applied strain from the pump. This corresponds to a 0.4% change in  $k_{\text{eff}}$ . Here, the gain is defined as the ratio of the response with and without pumping:  $G = \frac{A_{\text{pump-on}}}{A_{\text{pump-off}}}$ . Figure 4A illustrates an example of two Lorentzian responses with the pump on and off ( $A_{\text{pump-on}} = 95.6$  nV and  $A_{\text{pump-off}} = 33.1$  nV), yielding a gain of 2.9. In this coupled oscillator structure, the maximum phase-sensitive gain (19, 22) is found to be 3.3 at a relative phase of  $0^\circ$ . At a relative phase of  $90^\circ$ , parametric attenuation is observed as expected (Fig. 4B). In the experimental setup, the phase between the drive and pump signals can be locked because they represent  $f$  and its harmonic  $2f$ . The phase locking between the two signals is monitored with the use of an oscilloscope. Figure 4C shows the measured phase and amplitude relationship between the two signals.

The mechanically coupled two-oscillator structure demonstrates a large number of frequency synchronization regions, as illustrated by Arnold's tongues. Furthermore, we demonstrate phase-sensitive mechanical amplification of small signals. Future work would involve an array of mechanically coupled nanomechanical oscillators with the ability to self-oscillate. Even though synchronization resulting from reactive coupling and nonlinear frequency pulling has been studied in a model of a large array (23), a comprehensive study of two coupled nanomechanical oscillators will elucidate further aspects of the data in our experiments.

Demonstration of a large number of synchronization regions provides exciting opportunities for practical realization of pattern recognition with the use of oscillator networks. Storage and retrieval of complex patterns through the corresponding synchronized states will enable the feasibility of constructing nanomechanical neurocomputers. Small size, high speed, and low power consumption in these structures further add to the fundamental benefit of an on-chip nanomechanical oscillator network with distributed on-chip signal processing at microwave frequencies (24). The advantage of such a device would be its scalable architecture, based on standard lithography and semiconductor processing techniques. Beyond neural network models, nanomechanical oscillator networks capable of individual-oscillator addressing and global cou-

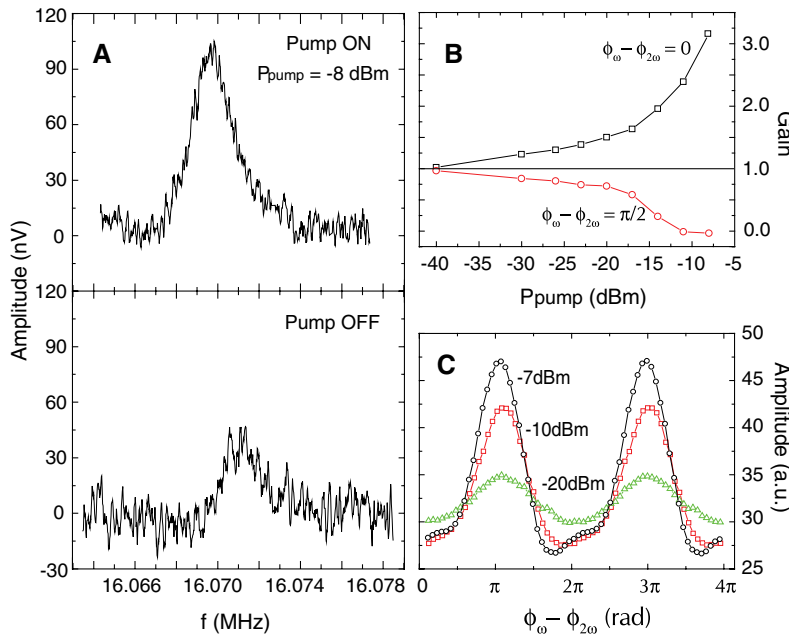


**Fig. 4.** Parametric amplification. (A) Response of the device structure with (top) and without (bottom) pumping.  $P_{\text{pump}}$ , pumping power. (B) Dependence of gain for varying  $P_{\text{pump}}$ . At a relative phase of  $0^\circ$  between driving and pumping signals, we measure parametric amplification, and, at a relative phase of  $90^\circ$ , we observe parametric attenuation. The maximum gain observed is 3.3 with possible indication of oscillation death.  $\phi_\omega - \phi_{2\omega}$  is the phase difference between the pump and drive signals. (C) Response as relative phase varies between the drive and the pump signal (monitored with an RF oscilloscope) for three different pumping powers. We observe a notable change in response as the two signals sweep from in phase to out of phase. a.u., arbitrary units.

pling could provide paradigms by enabling experimental realization of physical models that show phase transition, glassy states, and other collective behavior. If two coupled oscillators demonstrate such rich collective behaviors, a network of nanomechanical oscillators could possibly realize the complexity and intelligence, if not of the human brain subsystems, then at least those of pacemaker cells of a human heart or the rhythmic blinking of a congregation of fireflies.

#### References and Notes

1. A. T. Winfree, *The Geometry of Biological Time* (Springer-Verlag, New York, 1980).
2. S. Strogatz, *Syn: The Emerging Science of Spontaneous Order* (Hyperion, New York, 2003).
3. J. Buck, E. Buck, *Science* **159**, 1319 (1968).
4. C. S. Peskin, *Mathematical Aspects of Heart Physiology* (Courant Institute of Mathematical Sciences, New York University, New York, 1975).

5. S. F. Dermott, *Nature* **429**, 814 (2004).
6. C. Huygens, *Horologium Oscillatorium [The Pendulum Clock]* (Apud F. Muguet, Paris, 1673) [R. J. Blackwell, Transl. (Iowa State Univ. Press, Ames, IA, 1986)].
7. F. B. Mancoff, N. D. Rizzo, B. N. Engel, S. Tehrani, *Nature* **437**, 393 (2005).
8. S. Kaka *et al.*, *Nature* **437**, 389 (2005).
9. M. Zhaludtinov *et al.*, *Appl. Phys. Lett.* **78**, 3142 (2001).
10. K. L. Turner *et al.*, *Nature* **396**, 149 (1998).
11. V. I. Arnold, *Mathematical Methods of Classical Mechanics*, K. Vogtmann, A. Weinstein, Transl. (Springer-Verlag, New York, ed. 2, 1989).
12. E. V. Appleton, *Proc. Cambridge Philos. Soc.* **21**, 231 (1922).
13. B. van der Pol, *Philos. Mag.* **3**, 65 (1927).
14. E. M. Izhikevich, F. C. Hoppensteadt, *SIAM J. Appl. Math.* **63**, 1935 (2003).
15. C. Hayashi, *Nonlinear Oscillations in Physical Systems* (Princeton Univ. Press, Princeton, 1985).
16. A. Pikovsky, M. Rosenblum, J. Kurths, *Synchronization: A Universal Concept in Nonlinear Sciences* (Cambridge Univ. Press, Cambridge, 2001).
17. A. Gaidarzh, G. Zolfagharkhani, R. L. Badzey, P. Mohanty, *Phys. Rev. Lett.* **94**, 030402 (2005).

18. A. N. Cleland, M. L. Roukes, *Appl. Phys. Lett.* **69**, 2653 (1996).
19. D. Rugar, P. Grutter, *Phys. Rev. Lett.* **67**, 699 (1991).
20. D. W. Carr, S. Evoy, L. Sekaric, H. G. Craighead, J. M. Parpia, *Appl. Phys. Lett.* **77**, 1545 (2000).
21. M. Zhaludtinov *et al.*, *Appl. Phys. Lett.* **79**, 695 (2001).
22. A. N. Cleland, *New J. Phys.* **7**, 235 (2005).
23. M. C. Cross, A. Zumedieck, A. Lifshitz, J. L. Rogers, *Phys. Rev. Lett.* **93**, 224101 (2004).
24. R. L. Badzey, P. Mohanty, *Nature* **437**, 995 (2005).
25. This work was supported by NSF under grant number CCF-0432089 and partially under grant number DMR-0449670. We thank N. Kopel, Y. D. Park, J. Wei, and M. Grifoni for their valuable comments.

#### Supporting Online Material

www.sciencemag.org/cgi/content/full/316/5821/95/DC1  
Materials and Methods  
SOM Text  
Figs. S1 to S5  
References

8 November 2006; accepted 14 February 2007  
10.1126/science.1137307

# Giant Fluctuations of Coulomb Drag in a Bilayer System

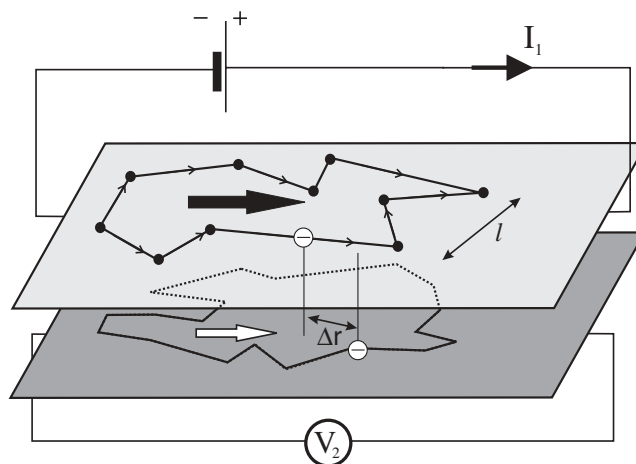
A. S. Price,<sup>1</sup> A. K. Savchenko,<sup>1\*</sup> B. N. Narozhny,<sup>2</sup> G. Allison,<sup>1</sup> D. A. Ritchie<sup>3</sup>

The Coulomb drag in a system of two parallel layers is the result of electron-electron interaction between the layers. We have observed reproducible fluctuations of the drag, both as a function of magnetic field and electron concentration, which are a manifestation of quantum interference of electrons in the layers. At low temperatures the fluctuations exceed the average drag, giving rise to random changes of the sign of the drag. The fluctuations are found to be much larger than previously expected, and we propose a model that explains their enhancement by considering fluctuations of local electron properties.

In conventional measurements of the resistance of a two-dimensional (2D) layer, an electrical current is driven through the layer and the voltage drop along the layer is measured. In contrast, Coulomb drag studies are performed on two closely spaced but electrically isolated layers, where a current  $I_1$  is driven through one of the layers (active layer) and the voltage drop  $V_2$  is measured along the other (passive) layer (Fig. 1). The origin of this voltage is electron-electron ( $e-e$ ) interaction between the layers, which creates a “frictional” force that drags electrons in the second layer. The ratio of this voltage to the driving current  $R_D = -V_2/I_1$  (the drag resistance) is a measure of  $e-e$  interaction between the layers. The measurement of Coulomb drag in systems of parallel layers was first proposed in (1, 2) and later realized in a number of experiments (3–7) [for a review, see (8)].

Because Coulomb drag originates from  $e-e$  interactions, it has become a sensitive tool for their study in many problems of contemporary condensed-matter physics. For example, Coulomb drag has been used in the search for Bose-condensation of interlayer excitons (9), the metal-insulator transition in 2D layers (10), and Wigner crystal formation in quantum wires (11).

**Fig. 1.** Schematic showing the origin of the drag signal  $V_2$  induced by the current  $I_1$ . The fluctuations of the drag arise from the interference of electron waves in each layer, before the two electrons take part in the interlayer interaction.



<sup>1</sup>School of Physics, University of Exeter, Stocker Road, Exeter EX4 4QL, UK. <sup>2</sup>The Abdus Salam International Centre for Theoretical Physics, Strada Costiera 11, Trieste I-34100, Italy. <sup>3</sup>Cavendish Laboratory, University of Cambridge, Madingley Road, Cambridge CB3 0HE, UK.

\*To whom correspondence should be addressed. E-mail: a.k.savchenko@ex.ac.uk